Structural Behavior of Two-Cell Composite Rotor Blades With Elastic Couplings

Ramesh Chandra* Inderjit Chopra**

University of Maryland, College Park, MD

Abstract

This paper presents an analytical-cum-experimental study of the structural response of composite rotor blades with elastic couplings. Vlasov theory is expanded to analyze two-cell composite rotor blades made out of general composite laminates including the transverse shear deformation of the cross-section. Variation of shear stiffness along the contour of the section is included in the warping function. In order to validate this analysis, two-cell graphite-epoxy composite blades with extension-torsion coupling were fabricated using matched-die molding technique. These blades were tested under tip bending and torsional loads, and their structural response in terms of bending slope and twist was measured with a laser optical system. Good correlation between theory and experiment is achieved. Axial force induced twist rate of the order of 0.2 degree per inch length can be realized in extension-torsion coupled blades with a hygrothermally stable $[20/-70]_{2s}$ layup for potential applications in the design of tilt rotors.

Notation

c, t	Chord and thickness of blade
ℓ	Length of blade
n, s, z	Coordinate system for plate segment
x, y, z	Coordinate system for blade
u, v, w	Displacements in n, s, z directions, referring to plate segment
U, V, W	Displacements in x, y, z directions, referring to blade
$\varepsilon_s, \varepsilon_z, \varepsilon_{sz}$	Membrane strains referring to plate segment
k_s, k_z, k_{sz}	Bending curvature referring to plate segment
ϕ_x, ϕ_y, ϕ_z	Rotations about x, y, z axes, referring to blade
$\varepsilon_{xz}, \varepsilon_{yz}$	Transverse shear strains for the blade in xz & yz planes, respectively
φ	Warping function
λ	constraint warping parameter
$\sigma_s, \sigma_z, \sigma_{sz}$	Stress field referring to plate segment
N_s, N_z, N_{sz}	Stress resultants referring to plate segment
M_s, M_z, M_{sz}	Moment resultants referring to plate segment
N	Axial force referring to blade
M_x, M_y	Bending moments referring to blade
V_x, V_y	Shear forces in x, y directions, referring to blade
T	Torsion moment referring to blade
M_ω	Bimoment (or warping moment) referring to blade
K_{ij}	Stiffness matrix for blade
$\overline{T}$	Applied torsion at tip of blade
P	Applied force at tip of blade
F	Axial force at the tip of blade
E_ℓ, E_t	Young's moduli of plies in principal directions
$\mu_{\ell t}$	Poisson's ratio of plies in principal plane
$G_{\ell t}$	Shear modulus of plies in principal plane
$(\ )'$	Differentiation with respect to z coordinate of blade

Presented at the Seventeenth European Rotorcraft Forum, Berlin, Germany, Sept. 24-27, 1991.
* Research Associate, Department of Aerospace Engineering
** Professor, Department of Aerospace Engineering

Introduction

With the application of high performance composite materials, the design feasibility of advanced rotor systems such as hingeless and bearingless rotors is becoming a reality. Superior fatigue characteristics and flexibility to tailor structural characteristics are the key factors for the growing application of composites in the rotorcraft industry. Because of the non-availability of validated composite analytical models, an extreme level of conservatism is used in rotorcraft design, and the potential benefits of structural couplings due to composites are not exploited at this time. Analyses of composite blade structures are more involved because nonclassical phenomena such as section warping and transverse shear related coupling become significant. For the full exploration of composites to improve the performance of current helicopters and also to meet many challenging missions of future helicopters, it is necessary to develop and validate analyses of composite blades with elastic couplings.

Helicopter rotor blades are slender and are normally modeled as elastic beams. Research studies on the modeling of coupled composite beams can be classified into four categories: solid rectangular cross-section, open section, single-cell closed section, and multi-cell aerofoil section.

References [1] -[4] investigated solid cross-section composite beams. Johnson [1] presented bending-torsion behavior of anisotropic beams in the small deflection regime under static loads. In that investigation, a variational method was used to predict the effective bending stiffness of bending-torsion coupled beams. Minguet and Dugundji [2, 3] presented an analytical-experimental study of composite beams in the large deflection regime under static and dynamic loading conditions. The large deflection analysis used Euler angles to include arbitrarily large deformation without the need for ordering scheme. For their dynamic analysis, small amplitude vibrations about the static deflected position of the beam were calculated using an influence coefficient method together with a finite difference solution. Calculated results were correlated satisfactorily with measured values for several composite coupled beams. Laulusa [4] conducted a theoretical and experimental investigation of composite beams under large deflection regime and rotating conditions. The analysis was based upon a finite element technique. The influence of pretwist and warping deformation was included. Fair correlation between theory and experiment for isotropic beams with initial twist was observed.

Under the category of open-section composite beams, Chandra and Chopra [5, 6, 7] presented a theoretical-cum-experimental study on static and dynamic behavior of composite I-beams. Such open-section composite beams are routinely used in the construction of flexbeams of a bearingless rotor. Their basic analysis was an extension of Vlasov theory [8, 9] for beams made out of general composite laminates, including transverse shear deformation. In the dynamic analysis, the Galerkin method was used to predict rotating free vibration characteristics of coupled composite I-beams. An in-vacuo rotor test facility was used to provide rotating vibration data for correlation to the analytical predictions. Graphite-epoxy and Kevlar-epoxy beams were built and tested for static and vibration characteristics. Modeling of constrained warping effects and general layered composite lamination of wall of composite open-section beams was considered mandatory to predict their structural response. Rehfield and Atilgan [10] presented a buckling analysis of composite open-section beams. They included transverse shear deformation, but neglected the bending stiffness of the wall.

Hong and Chopra [11] studied the aeroelastic stability of hingeless rotor blades where the blade was modeled as a single-cell, thin wall, rectangular section composite beam. That investigation showed a significant influence of elastic couplings caused by layered composites on blade dynamics. Chandra et al [12] evaluated the composite structural model of Ref [11] by finite-element and experimental techniques for bending-torsion and extension-torsion coupled composite box beams. The poor correlation was attributed to inadequate modeling of nonclassical effects. Smith and Chopra [13] introduced transverse shear effects into the structural model of Ref [11]. Also, the variation of shear stiffness along the contour of the section was incorporated in the warping function. These refinements helped improve the correlation of predicted static response results with measured values. Chandra and Chopra [14] presented theoretical and experimental vibration characteristics of composite box beams under rotation. In that study the analysis was based upon the structural model of Ref [13] and the Galerkin method was used to predict natural frequencies and mode shapes of composite box beams with couplings. Predicted frequencies and mode shapes correlated satisfactorily with measured values for several composite box beams.

Rehfield et al [15] presented a beam theory for composite single-cell box beams with extension-twist couplings. The analytical model used contour analysis and neglected the local bending stiffness of the thin-walled beams. Experimental correlation was provided for extension-torsion coupled beams. That study showed the importance of transverse shear deformation for composite box beam analysis. Hodges et al [16] presented a theoretical study on free-vibration characteristics of composite beams without rotation. The analysis was based upon the structural model of Ref [15]. The equations of motion were solved by exact integration and mixed finite element methods. Rehfield et al [17] extended their earlier structural modeling to multi-cell composite beams.

Kosmatka [18] presented the static structural behavior of thin-walled composite beams with initial twist. Single-cell D-section beams with initial twist were analyzed. Importance of initial twist in modeling of rotor blades was pointed out. Nixon [19] examined the elastic twist requirements for full-scale extension-twist coupled tilt-rotor blades. He used the beam theory of Ref [15] to predict the elastic twist of circular composite tubes representative of tilt rotor blades under torsion and axial loads. The potential of elastic couplings due to composites was shown to improve tilt rotor performance.

The above mentioned studies show that the important nonclassical effects in the analysis of thin-walled composite beams are: cross-section warping, and transverse shear related elastic couplings. Most analyses are confined to single-cell, thin-walled, box beams. The objective of the present investigation is to formulate a structural analysis of a two-cell composite rotor blade in the regime of small deflection theory including these nonclassical effects, and then to validate the analysis by experiments. The present analysis is an extension of the authors' earlier work [5] related to open-section composite beams.

Analysis

In this paper, Vlasov theory is expanded to analyze a two-cell spar-skin rotor blade made out of general composite laminates. Transverse shear effects are also included. The essence of this theory is the reduction of two-dimensional stress and displacement fields (associated with plate/shell segments of the blade) to one-dimensional stresses and displacements identified with the blade. The six generalized blade displacements are determined from the plate/shell displacements through geometric considerations, whereas, the generalized blade forces and their equilibrium equations are obtained by invoking the principle of virtual work.

The present analysis uses three coordinate systems: an orthogonal right-handed Cartesian coordinate system (x, y, z) for the blade, Fig. 1a; an orthogonal coordinate system (n, s, z), for any plate segment of the blade, Fig. 1b where the n-axis is normal to the mid surface of any plate segment, the s-axis is tangential to the mid surface and is along the contour line of the blade cross-section, and the z-axis is along the longitudinal axis of blade; and a contour coordinate system s, where 's' is measured along the contour line of the cross-section from a judiciously selected origin, Fig. 1d. The seven generalized blade forces V_x, V_y, V_z, M_x, M_y, T and M_ω are shown in Fig. 1c. The torsional moment T consists of unconstrained warping torsion (Saint Venant torsion), and constrained warping torsion (Vlasov torsion). As shown later, the Vlasov torsion and bimoment M_ω are related to each other. The stress resultants, moment resultants and transverse shear forces acting on any general plate segment of blade are shown in Fig. 1b. The plate stress and displacement fields are functions of s and z.

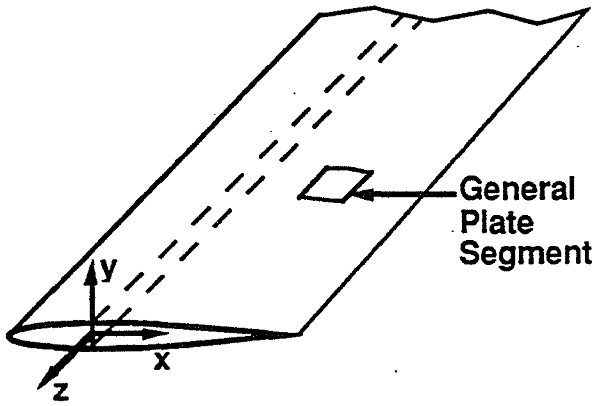

Fig. 1a. Cartesian coordinates in rotor blade

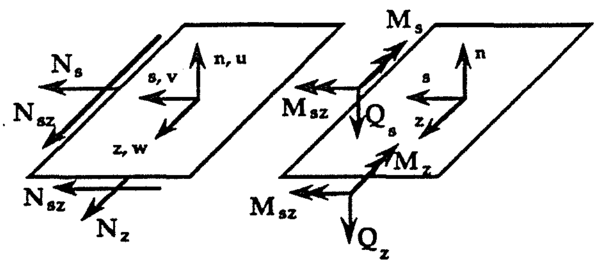

Fig. 1b. Stress and moment resultants acting on any general plate segment of rotor blade.

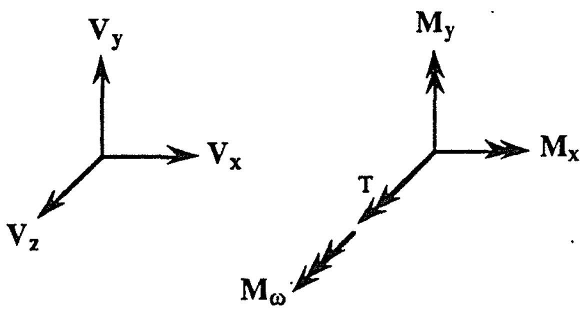

Fig. 1c. Generalized forces for rotor blade.

Fundamental Assumptions

Three basic assumptions used in the present theory are:

(1) The contour (mid-line of the plate segments) of a cross section does not deform in its plane. This means that the inplane warping of the cross-section is neglected and the normal strain ε_s in the contour direction is neglected in comparison with the normal axial strain ε_z. This assumption was introduced by Vlasov [8].

(2) The normal stress σ_s is neglected in comparison with σ_z.

(3) Any general plate/shell segment of the blade behaves as a thin plate. This implies that the transverse shear deformation of the plate/shell segment is not accounted for, though the transverse shear deformation of the blade is considered.

(4) A general plate/shell segment of the blade is governed by linear classical laminated plate theory.

These assumptions imply that the nonzero membrane strains and bending curvatures for the plate segment are ε_z, ε_{sz}, k_z and k_{sz}.

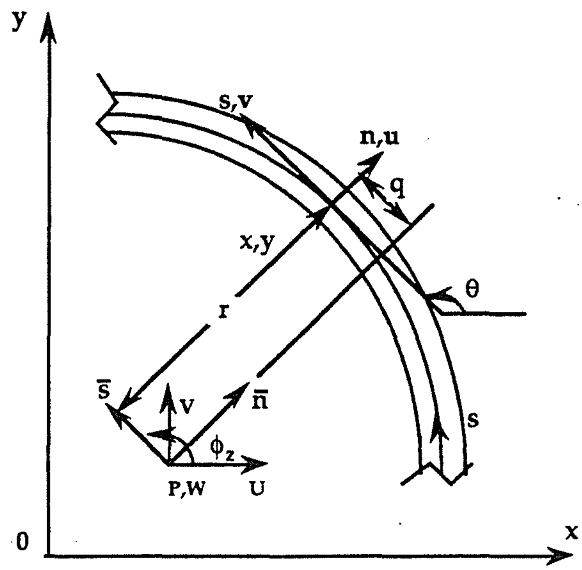

Fig. 1d. Pictorial definitions of blade displacements and rotations.

Kinematics

In the present formulation each blade segment is idealized as a thin laminated composite plate.

From geometric considerations Fig. 1d, the plate displacements u(s,z) and v(s,z) are related to the blade displacements U,V and ϕ_z as:

$$u(s,z) = U(z)\sin\theta(s) - V(z)\cos\theta(s) - q(s)\phi_z(z) \quad (1)$$

$$v(s,z) = U(z)\cos\theta(s) + V(z)\sin\theta(s) + r(s)\phi_z(z) \quad (2)$$

where, r, q and θ are shown in Fig. 1d. w(s,z) is obtained using the following shear strain-displacement relation:

$$\varepsilon_{sz} = w_{,s} + v_{,z} \quad (3)$$

The shear strain ε_{sz} consists of two components; one due to transverse shear effects and the other due to torsion. Hence, ε_{sz} is given by:

$$\varepsilon_{sz} = \varepsilon_{xz}\cos\theta + \varepsilon_{yz}\sin\theta + \varepsilon_{sz}^{(s)} \quad (4)$$

It is assumed that shear strain $\varepsilon_{sz}^{(s)}$ distribution in the contour direction is similar to the one corresponding to the St. Venant torsion.

From Ref. [9], $\varepsilon_{sz}^{(s)}$ is given by:

$$\varepsilon_{sz}^{(s)}(s,z) = \frac{F(s)}{t(s)}\phi_z'(z) \quad (5)$$

F(s) controls the variation of this shear strain along the contour of the blade cross-section. In order to account for variation of shear modulus G along the contour, equation (5) is rewritten as:

$$\varepsilon_{sz}^{(s)}(s,z) = \frac{G_s(s)}{Gt}\phi_z'(z) \quad (6)$$

where, $G_s(s) = F(s)G(s)$

$G_s(s)$ is determined using compatibility condition for warping deformation [9]. Figure 2 shows a two-cell blade section. It has two circuits for shear flow with five branches. Invoking the condition of net warping deformation over each circuit to be zero, the following equation is obtained:

$$\oint_i dw = \oint_i \frac{\partial w}{\partial s} ds = 0, \; i = 1,2 \quad (7)$$

Using equations (2), (3) and (4) in equation (7),

$$\oint \frac{G_s}{Gt} ds = 2A_i \quad (8)$$

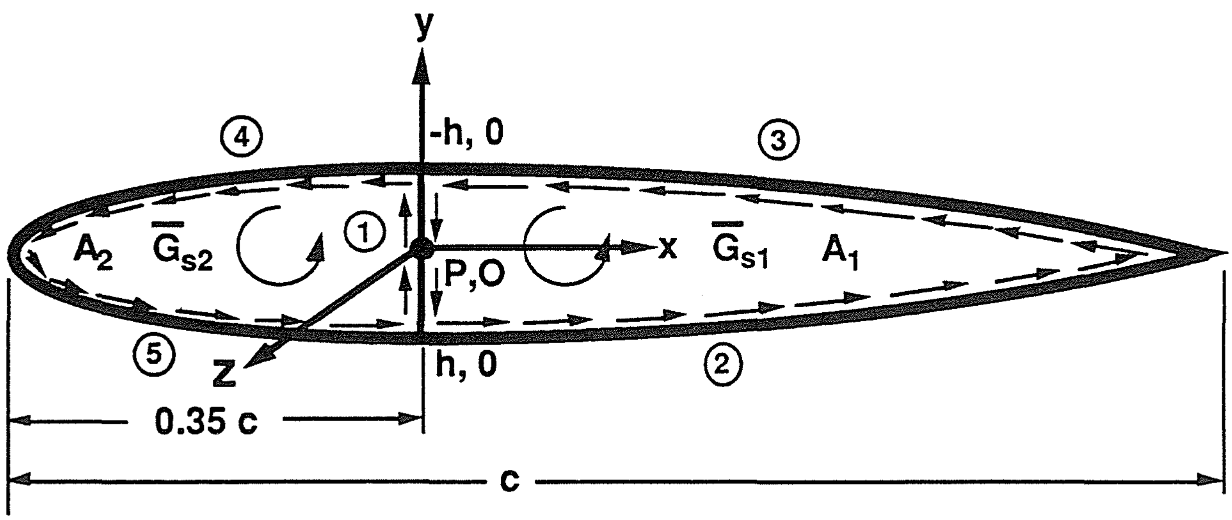

Fig. 2. Schematic of two-cell blade section.

where, $A_i = \oint_i r\, ds$

For a single-cell section, G_s is obtained from relation (8) as follows:

$$G_s = \frac{2A}{\oint \frac{1}{G\,t} ds}$$

Equation (8) is used to compute $G_s(s)$. $\overline{G}_{s1}$ and $\overline{G}_{s2}$ are the values of G_s associated with circuits and G_{s1} to G_{s5} are the values of G_s associated with branches. From Figure 2,

$$\begin{aligned} G_{s1} &= \overline{G}_{s1} - \overline{G}_{s2} \\ G_{s2} &= \overline{G}_{s1} \\ G_{s3} &= \overline{G}_{s1} \\ G_{s4} &= \overline{G}_{s2} \\ G_{s5} &= \overline{G}_{s2} \end{aligned} \tag{9}$$

Using relation (8) for two circuits,

$$\overline{G}_{s1}\left[\int_{-h}^{h} \frac{ds_1}{G_1 t_1} + \int_0^{p_1} \frac{ds_2}{G_2 t_2} + \int_0^{p_1} \frac{ds_3}{G_3 t_3}\right] - \overline{G}_{s2} \int_{-h}^{h} \frac{ds_1}{G_1 t_1} ds_1 = 2\, A_1 \tag{10}$$

$$\overline{G}_{s2}\left[\int_{-h}^{h} \frac{ds_1}{G_1 t_1} + \int_0^{p_2} \frac{ds_4}{G_4 t_4} + \int_0^{p_2} \frac{ds_5}{G_5 t_5}\right] - \overline{G}_{s1} \int_{-h}^{h} \frac{ds_1}{G_1 t_1} ds_1 = 2\, A_2 \tag{11}$$

where, $p_1 = \int_{0.35c}^{c} ds$, $p_2 = \int_0^{0.35c} ds$

$$A_1 = 2\int_{0.35c}^{c} y\, dx, \quad A_2 = 2\int_0^{0.35c} y\, dx$$

Solving equations (10) and (11),

$$\overline{G}_{s1} = \frac{A_1\left(\frac{h}{A_{66}^{(w)}} + \frac{p_2}{A_{66}^{(sp)}}\right) + A_2 \frac{h}{A_{66}^{(w)}}}{\left(\frac{h}{A_{66}^{(w)}} + \frac{p_1}{A_{66}^{(sk)}}\right)\left(\frac{h}{A_{66}^{(w)}} + \frac{p_2}{A_{66}^{(sp)}}\right) - \left(\frac{h}{A_{66}^{(w)}}\right)^2} \tag{12}$$

$$\overline{G}_{s2} = \frac{A_2\left(\frac{h}{A_{66}^{(w)}} + \frac{p_1}{A_{66}^{(sk)}}\right) + A_1 \frac{h}{A_{66}^{(w)}}}{\left(\frac{h}{A_{66}^{(w)}} + \frac{p_1}{A_{66}^{(sk)}}\right)\left(\frac{h}{A_{66}^{(w)}} + \frac{p_2}{A_{66}^{(sp)}}\right) - \left(\frac{h}{A_{66}^{(w)}}\right)^2} \tag{13}$$

Using relations (2), (3), (4) and (6), w is obtained as:

$$w = W + x\phi_x + y\phi_y - \varphi\phi_z' \tag{14}$$

where the warping function, φ, is equal to:

$$\varphi = \int_0^s \left(r - \frac{G_s}{Gt}\right) ds \tag{15}$$

It is important to note that the second term in the parenthesis of the integral is zero for an open section.

$$\begin{aligned} \phi_x &= \varepsilon_{xz} - U' \\ \phi_y &= \varepsilon_{yz} - V' \end{aligned} \tag{16}$$

Plate strain ε_z is related by the following equation:

$$\varepsilon_z = w_{,z} \tag{17}$$

Using relations (14) and (17), ε_z is obtained as:

$$\varepsilon_z = W' + x\phi_x' + y\phi_y' - \varphi\phi_z'' \tag{18}$$

Similarly k_z and k_{zs} are obtained as:

$$k_z = -\sin\theta\,\phi_x' + \cos\theta\,\phi_y' - q\phi_z'' + \varepsilon_{xz}'\sin\theta - \varepsilon_{yz}'\cos\theta \tag{19}$$

$$k_{zs} = -2\phi_z' \tag{20}$$

Thus the non-zero membrane strains and bending curvatures in the plate segment are given by relations (18), (4), (19) and (20).

Plate Stress Field

Using classical laminated plate theory, the stress resultants and moment resultants are:

$$\begin{aligned} N_z &= A_{11}\varepsilon_z + A_{16}\varepsilon_{zs} + B_{11}k_z + B_{16}k_{zs} \\ N_{zs} &= A_{16}\varepsilon_z + A_{66}\varepsilon_{zs} + B_{16}k_z + B_{66}k_{zs} \\ M_z &= B_{11}\varepsilon_z + B_{16}\varepsilon_{zs} + D_{11}k_z + D_{16}k_{zs} \\ M_{zs} &= B_{16}\varepsilon_z + B_{66}\varepsilon_{zs} + D_{16}k_z + D_{66}k_{zs} \end{aligned} \tag{21}$$

where [A], [B] and [D] are defined in Appendix A.

Here, the flanges and web of D-spar and blade skin are treated as general composite laminates.

Blade Forces and Their Equilibrium Equations

The generalized forces of blade and their equilibrium equations are derived by applying the principle of virtual work. This approach is similar to the one used by Gjelsvik [9] except now the transverse shear deformation of the blade is taken into account. The external work done by the plate forces during a displacement of the cross-section, is:

$$W_e = \int_s [N_z w + M_z u' + N_{zs} v - Q_z u - M_{zs}\phi_z]\, ds + \sum_{\text{branches}} (M_{zs}^j u^j - M_{zs}^i u^i) \tag{22}$$

Using relations (1), (2), and (14) and taking the variation of W_e,

$$\delta W_e = N\delta W + V_x\delta U + V_y\delta V + T\delta\phi_z + M_\omega\delta\phi_z' + M_y\delta\phi_x + M_x\delta\phi_y + F_x\delta\varepsilon_{xz} + F_y\delta\varepsilon_{yz} \tag{23}$$

where $N = \int_s N_z\, ds$ (24)

$$V_x = \int_s (N_{zs}\cos\theta - Q_z\sin\theta)\, ds + \sum_{\text{branches}} (M_{zs}^j \sin\theta^j - M_{zs}^i \sin\theta^i) \tag{25}$$

$$V_y = \int_s (N_{zs}\sin\theta + Q_z\cos\theta)\, ds + \sum_{\text{branches}} (-M_{zs}^j \sin\theta^j + M_{zs}^i \sin\theta^i) \tag{26}$$

$$T = \int_s (N_{zs}r + Q_z q - M_{zs})\, ds + \sum_{\text{branches}} (-M_{zs}^j q^j + M_{zs}^i q^i) \tag{27}$$

$$M_\omega = -\int_s (N_z\varphi + M_z q)\, ds \tag{28}$$

$$M_x = \int_s (N_z y + M_z\cos\theta)\, ds \tag{29}$$

$$M_y = \int_s (N_z x - M_z\sin\theta)\, ds \tag{30}$$

$$F_x = \int_s M_z\sin\theta\, ds \tag{31}$$

$$F_y = -\int_s M_z\cos\theta\, ds \tag{32}$$

It is difficult to compute the generalized blade forces V_x, V_y and T from relations (25), (26) and (27) because of the contributions from different branches. These are simplified by using equilibrium equations of plate forces [9]:

$$V_x = -M_y' \tag{33}$$

$$V_y = M_x' \tag{34}$$

$$T = T_s + T_\omega \tag{35}$$

where T_s is Saint Venant Torsion (free warping) and T_ω is Vlasov Torsion (constrained warping). These are defined as:

$$T_s = -2\int_s M_{sz}\, ds + \int_s N_{sz}\frac{G_s}{Gt} ds \tag{36}$$

It is to be noted that the second term in the equation of St. Venant torsion is zero for an open section.

$$T_\omega = \int_s (N_{zs}\, r + M_z' q)\, ds \tag{37}$$

By using the plate equilibrium equation, relation (37) is simplified to:

$$T_\omega = -M_\omega' \tag{38}$$

This gives the relationship between Vlasov torsion and warping moment (or bimoment).

The external virtual work done by the applied loadings on the plate is:

$$n\delta W + v_x\delta U + v_y\delta V + t\delta\phi_z + m_\omega\delta\phi_z'' + m_y\delta\phi_x + m_x\delta\phi_y + f_x\delta\varepsilon_{xz} + f_y\delta\varepsilon_{yz} \tag{39}$$

where n, v_x, v_y, t, m_ω, m_y, m_x, f_x and f_y are generalized load intensities on the blade, derived from the loadings on shell [9].

The strain energy, Π, is given as

$$\Pi = \frac{1}{2}\int_s (N_z\,\varepsilon_z + N_{zs}\,\varepsilon_{zs} + M_z\,k_z + M_{zs}\,k_{zs})\, ds \tag{40}$$

Using the relations between blade forces and shell forces, the strain energy becomes

$$\Pi = \frac{1}{2}[NW' + M_y\phi_x' + M_x\phi_y' + T\phi_z' + M_\omega\phi_z'' + F_x\varepsilon_{xz}' + F_y\varepsilon_{yz}' + G_x\varepsilon_{xz} + G_y\varepsilon_{yz}] \tag{41}$$

The internal virtual work, W_i, is obtained from the strain energy as:

$$-W_i = NW' + M_y\phi_x' + M_x\phi_y' + T\phi_z' + M_\omega\phi_z'' + F_x\varepsilon_{xz}' + F_y\varepsilon_{yz}' + G_x\varepsilon_{xz} + G_y\varepsilon_{yz} \tag{42}$$

where $G_x = \int_s N_{zs}\cos\theta\, ds$ (43)

$$G_y = \int_s N_{zs}\sin\theta\, ds \tag{44}$$

Equilibrium equations for blade forces are obtained by considering a blade element and equating the external work to internal work for any virtual displacement. Thus these equations are:

$$V_x' + v_x = 0 \tag{45}$$

$$V_y' + v_y = 0 \tag{46}$$

$$N' + n = 0 \tag{47}$$

$$T' + t = 0 \tag{48}$$

$$M_\omega' + T - T_s + m_\omega = 0 \tag{49}$$

$$M_y' + V_x + m_y = 0 \tag{50}$$

$$M_x' - V_y + m_x = 0 \tag{51}$$

$$F_x' - G_x + f_x = 0 \tag{52}$$

$$F_y' - G_y + f_y = 0 \tag{53}$$

By eliminating V_x, V_y and T, the equations are reduced to six equations:

$$N' + n = 0 \tag{54}$$

$$M_y'' + m_y' - v_x = 0 \tag{55}$$

$$M_x'' + m_x' + v_y = 0 \tag{56}$$

$$M_\omega'' - T_s' + m_\omega' - t' = 0 \tag{57}$$

$$F_x' - G_x + f_x = 0 \tag{58}$$

$$F_y' - G_y + f_y = 0 \tag{59}$$

Blade Force - Displacement Relations

There are 9 generalized blade forces namely N, M_y, M_x, M_ω, T_s, F_x, F_y, G_x and G_y appearing in the above equations. These 9 generalized forces are related to 6 generalized displacements. Using plate stress-strain relations (21) and plate strain-beam displacement relations (18), (4), (19) and (20), the following relations between the generalized bar forces and displacement are obtained:

$$\begin{bmatrix} N \\ M_x \\ -M_y \\ M_\omega \\ T_s \\ G_x \\ G_y \\ F_x \\ F_y \end{bmatrix} = \begin{bmatrix} K_{11} & K_{12} & K_{13} & K_{14} & K_{15} & K_{16} & K_{17} & K_{18} & K_{19} \\ K_{12} & K_{22} & K_{23} & K_{24} & K_{25} & K_{26} & K_{27} & K_{28} & K_{29} \\ K_{13} & K_{23} & K_{33} & K_{34} & K_{35} & K_{36} & K_{37} & K_{38} & K_{39} \\ K_{14} & K_{24} & K_{34} & K_{44} & K_{45} & K_{46} & K_{47} & K_{48} & K_{49} \\ K_{15} & K_{25} & K_{35} & K_{45} & K_{55} & K_{56} & K_{57} & K_{58} & K_{59} \\ K_{16} & K_{26} & K_{36} & K_{46} & K_{56} & K_{66} & K_{67} & K_{68} & K_{69} \\ K_{17} & K_{27} & K_{37} & K_{47} & K_{57} & K_{67} & K_{77} & K_{78} & K_{79} \\ K_{18} & K_{28} & K_{38} & K_{48} & K_{58} & K_{68} & K_{78} & K_{88} & K_{89} \\ K_{19} & K_{29} & K_{39} & K_{49} & K_{59} & K_{69} & K_{79} & K_{89} & K_{99} \end{bmatrix} \begin{bmatrix} W' \\ \phi_y' \\ \phi_x' \\ \phi_z'' \\ \phi_z' \\ \varepsilon_{xz} \\ \varepsilon_{yz} \\ \varepsilon_{xz}' \\ \varepsilon_{yz}' \end{bmatrix} \tag{60}$$

where K_{ij} coefficients are given in Appendix A.

It is interesting to note that for flanges and webs made out of general laminates, the [K] matrix is fully populated, implying the existence of such couplings as extension-bending, extension-twist, extension-shear, bending-twist, bending-shear, etc.

Extension-Torsion Coupled Blades Under Bending and Torsional Loads

Figure 3 shows the lay-up details for extension-torsion coupled blades. Note that the spar has [0/θ] lay-up whereas the skin has [+θ/-θ] lay-up. The θ layer in the spar causes antisymmetry with respect to the mid-plane and hence creates extension-torsion coupling in the blade. For these blades, the relations (60) are simplified to:

$$\begin{Bmatrix} N \\ T_s \end{Bmatrix} = \begin{bmatrix} K_{11} & K_{15} \\ K_{15} & K_{55} \end{bmatrix} \begin{Bmatrix} W' \\ \phi_z' \end{Bmatrix} \tag{61}$$

$$\begin{Bmatrix} M_x \\ G_x \end{Bmatrix} = \begin{bmatrix} K_{22} & K_{26} \\ K_{26} & K_{66} \end{bmatrix} \begin{Bmatrix} \phi_y' \\ \varepsilon_{xz} \end{Bmatrix} \tag{62}$$

$$\begin{Bmatrix} -M_y \\ G_y \end{Bmatrix} = \begin{bmatrix} K_{33} & K_{37} \\ K_{37} & K_{77} \end{bmatrix} \begin{Bmatrix} \phi_x' \\ \varepsilon_{yz} \end{Bmatrix} \tag{63}$$

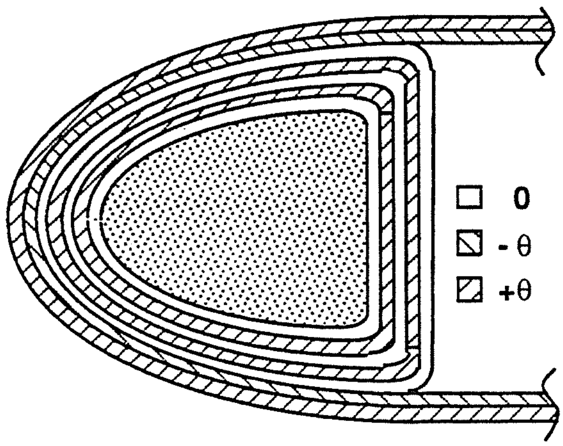

Figure 3. Lay-up of Extension-Torsion Coupled Blades

For blades subjected to tip torsional load $\overline{T}$, the twist is given by:

$$\phi_z = \frac{K_{11}}{K_{11}K_{55} - K_{15}^2}\,\bar{T}z \tag{64}$$

For blades subjected to axial force F, the induced twist rate is given by:

$$\phi_z' = \frac{K_{15}}{K_{11}K_{55} - K_{15}^2}\,F \tag{65}$$

For blades subjected to tip bending load P, the bending slope ϕ_y is obtained from relation (62).

$$\phi_y = \frac{P}{K_{22}\left(1 - \dfrac{K_{26}^2}{K_{22}K_{66}}\right)}\left(\frac{z^2}{2} - \ell z\right) \tag{66}$$

From equation (66), the influence of bending-transverse shear coupling K_{26} is seen to decrease the bending stiffness, K_{22}.

Experiments

In order to validate the analysis, two-cell composite rotor blades with foam core were fabricated using a matched-die molding technique. The schematic of the fabrication process is given in Figure 4.

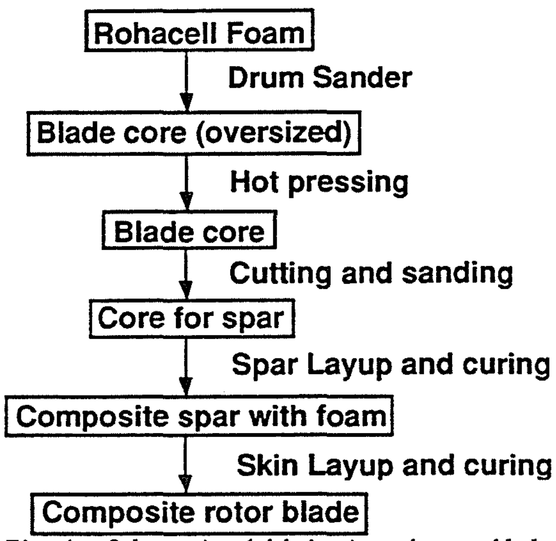

Fig. 4. Schematic of fabrication of rotor blade.

There are three important aspects of this process. These are: making of rigid foam core, making of foam filled spar and finally making of spar-skin-foam rotor blade. The rigid foam core is oversized by about 10-15 percent so that the required pressure could be applied to the composite layers while curing. The foam core in the required airfoil shape is built using compression molding technique. In this method, rough-machined ROHACELL blank foam is placed in a heated mold (350 F) and formed to the desired geometry by means of compression provided by fastening the mold. Figure 5 shows the schematic of this process.

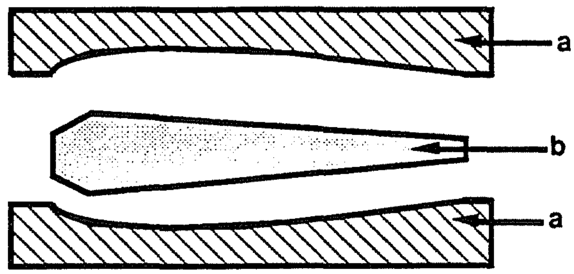

a) Heated mold
b) Rough-machined ROHACELL blank

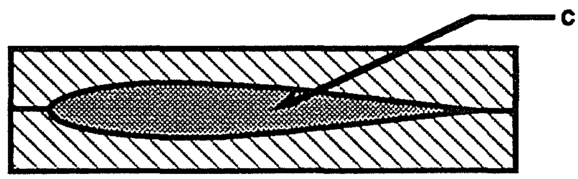

c) Finished ROHACELL core

Fig. 5. Fabrication of ROHACELL foam core.

This foam core is cut into two pieces to provide cores for D spar and trailing edge separately. First, a composite D spar is built using matched-die molding technique. For this, the desired number of composite prepreg layers are laid on to the foam core and each layer is compacted by means of a vacuum pump. The lay-up with foam is placed in the mold and the assembly is kept in an oven for curing. Thus, a D spar is fabricated. Figure 6 shows the schematic of this process. In order to make a two-cell blade, the cured spar and trailing edge are wrapped by [+θ/-θ] layers as skin, and vacuum compacted. This lay-up is kept in the mold and cured in oven. Figure 7 shows the schematic diagram of this process.

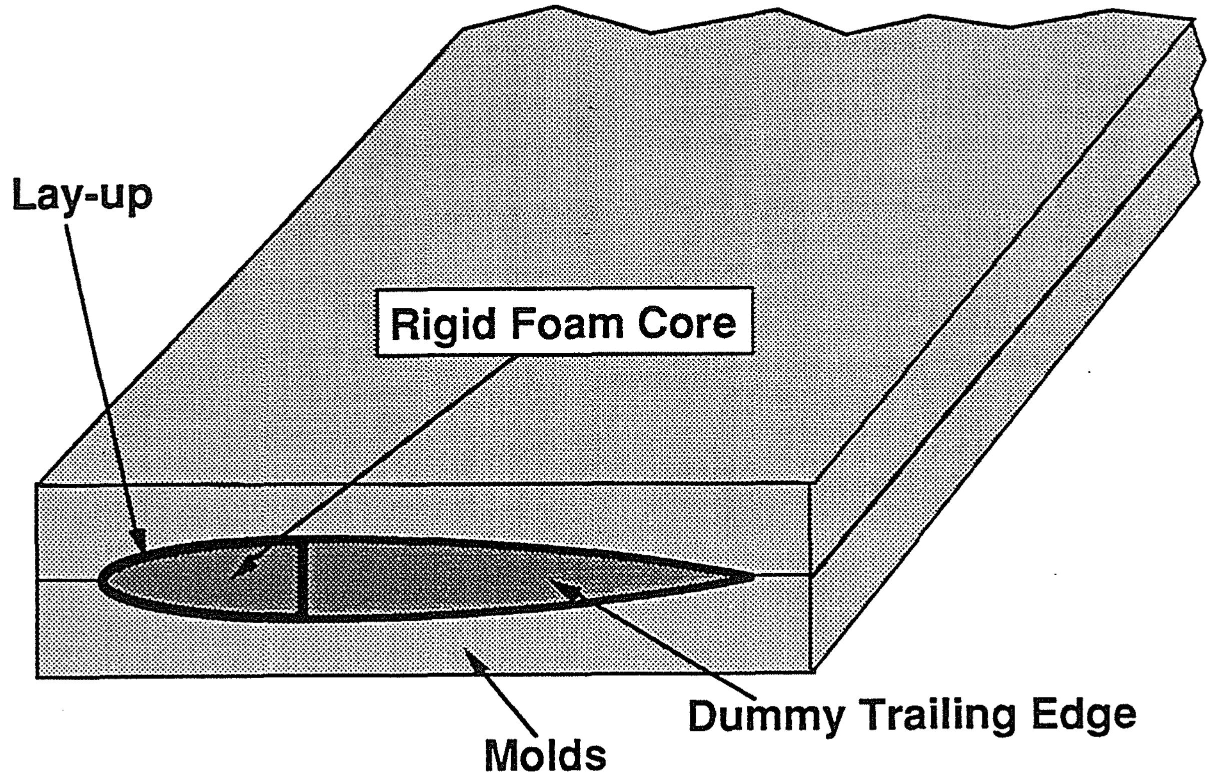

Fig. 6. Schematic of fabrication of D-spar.

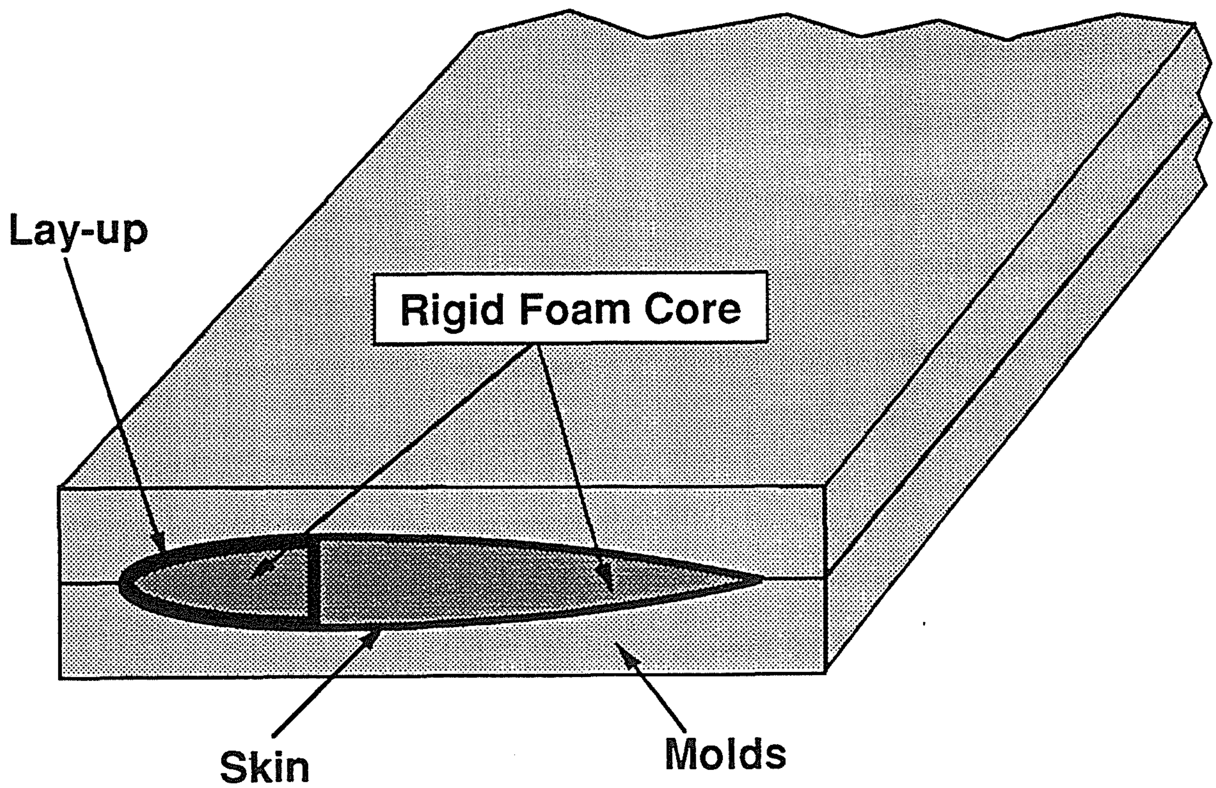

Fig. 7. Fabrication of rotor blade.

Several graphite-epoxy rotor blades of 28 in. length, 3 in. width and 0.36 in. thickness were fabricated in this manner. These were tested for their structural response under tip bending and torsional loads using a simple test set-up [12]. The structural response in terms of bending slope and twist was measured by using a laser optics system. Table 1 gives the details of the blades which were fabricated and tested. Figure 8 shows the details of clamped and loading ends of the blade. In order to simulate the clamped condition accurately, the clamped end was reinforced with additional composite layers .

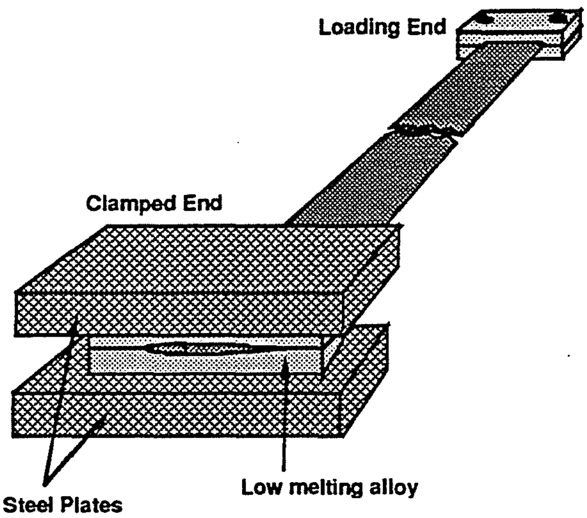

Fig. 8a. Details of clamped end of rotor blade.

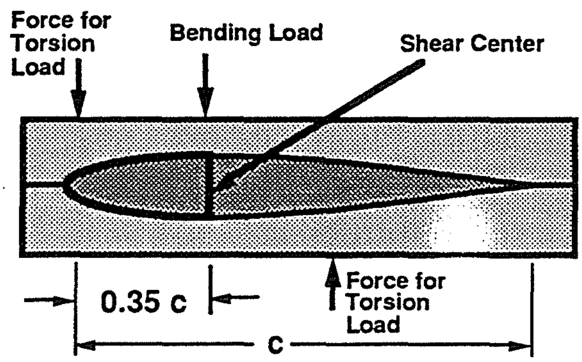

Fig. 8b. Details of loading end of rotor blade.

Results and Discussion

The present analysis is evaluated first for single-cell composite box beams and then validation studies are carried out for two-cell composite blade models.

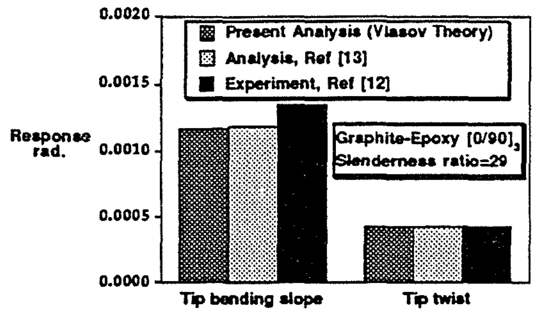

Fig. 9. Response of graphite-epoxy $[0/90]_3$ box beam under unit tip bending and torsional loads.

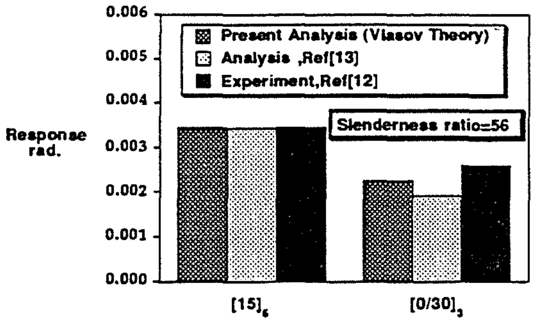

Figure 10. Tip twist of graphite-epoxy box beams under unit tip torsional load.

Single-cell Box Beams: Figure 9 shows the static structural response of graphite-epoxy box beams under unit tip bending and unit tip torsional loads. Predicted values are correlated with measured values reported in Ref. [12] and the calculated values of Ref. [13]. It represents a thin-walled cross-ply box beam of length 30 in. Present analysis predicts the tip bending slope and twist accurately. Figure 10 shows the tip twist of graphite-epoxy $[15]_6$ and $[0/30]_3$ box beams under unit tip torsional load. These beams have antisymmetry with respect to their mid-planes and have extension-torsion couplings. The results of the present analysis correlate better with experimental data for $[0/30]_3$ beams. Thus, the performance of the present analysis in predicting the static structural response of single-cell graphite-epoxy box beams under bending and torsional loads is very good.

Two-cell Blades with Extension-Torsion Couplings: Figure 11 shows the influence of fiber orientation on the induced twist rate of extension-torsion coupled blades. Blade 1 consists of unidirectional spar and ±15 skin. Blade 2 consists of $[0/15]_2$ spar and ±15 skin. Blade 3 consists of $[0/30]_2$ spar and ±30 skin. Blade 4 has $[0/45]_2$ spar and ±45 skin. Note the existence of small extension-torsion coupling in Blade 1 due to extension-twist coupling stiffness (B_{16}) of the skin. This blade will not show this coupling if the skin is modeled as a membrane. The maximum twist rate at an axial force of 1000 lbs. is about 0.040 deg./in. for Blade 2.

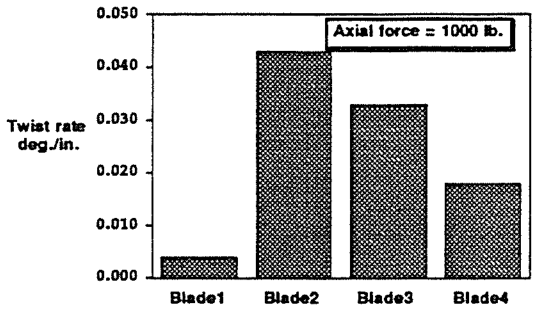

Fig. 11. Twist rate of extension-torsion coupled rotor blades under axial force.

Figure 12 shows the tip bending slope and twist of extension-torsion coupled blade (Blade 1) under tip bending and torsional loads. It is seen from this figure that the bending flexibility of this blade is about three times the torsional flexibility. Results corresponding to single-cell theory are obtained by neglecting the web and treating the blade section as a single cell. As expected, the two-cell analysis predicts higher stiffnesses as compared to single cell analysis, and experimental results are closer to two-cell analysis. Good correlation between two-cell analysis and experiment is noted.

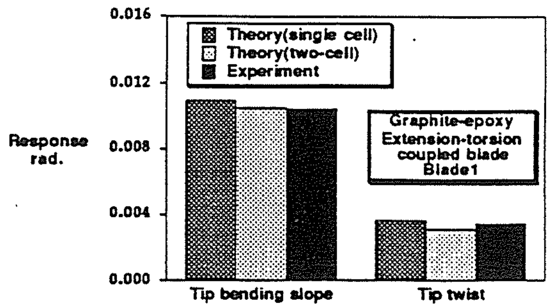

Figure 12. Response of extension-torsion coupled blade under unit bending and torsional loads (Blade 1).

Figure 13 shows similar results for Blade 2. This blade has ±15 skin and $[0/15]_2$ spar. Hence, the extension-twist coupling for this blade is due to B_{16} of skin and A_{16} and B_{16} of spar. Good correlation between two-cell analysis and experiment is achieved for this blade, also.

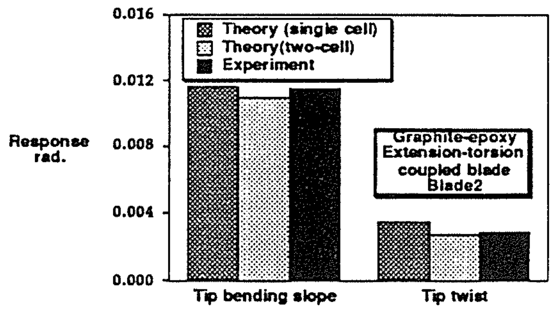

Figure 13. Response of extension-torsion coupled rotor blade under unit bending and torsional loads (Blade 2).

Figure 14 presents the response of Blade 3 under tip bending and torsional loads. This blade has ±30 skin and $[0/30]_2$ spar. Note the increase in torsional stiffness of this blade due to higher angle of fiber orientation. Satisfactory correlation of two-cell analysis with experimental data is observed for this blade.

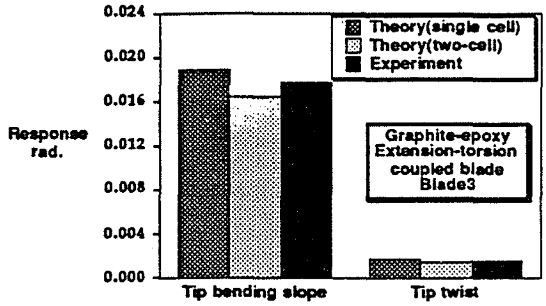

Figure 14. Response of extension-torsion coupled rotor blade under unit bending and torsional loads (Blade 3).

Figure 15 shows the response of Blade 4 under tip loadings. This blade has ±45 skin and $[0/45]_2$ spar. It is to be noted that the torsional stiffness in comparison with the bending stiffness is increased very substantially due to the higher angle of fiber orientation. Again, good correlation between two-cell analysis and experiment is achieved for this blade.

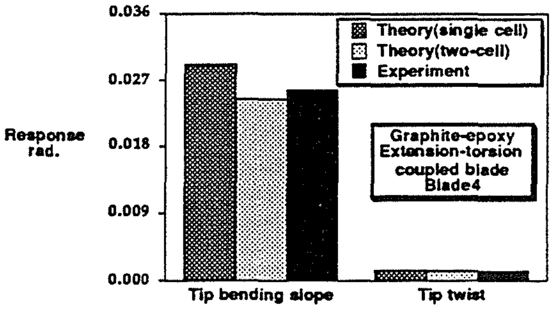

Figure 15. Response of extension-torsion coupled rotor blade under unit bending and torsional loads (Blade 4).

Figure 16 shows the influence of bending-transverse shear (BS) and extension-torsion (ET) couplings on tip bending slope and tip twist of extension-torsion coupled blades subjected to unit tip bending and torsional loads. Blade 5 consists of $[(20/-70)_2]_s$ spar and [20/-70] skin. It is to be noted that for Blade 5, tip bending slope is increased by 36% by bending-shear coupling and tip twist is increased by 26% by extension-torsion coupling. However, for Blade 1 to Blade 4, these couplings do not influence their structural response.

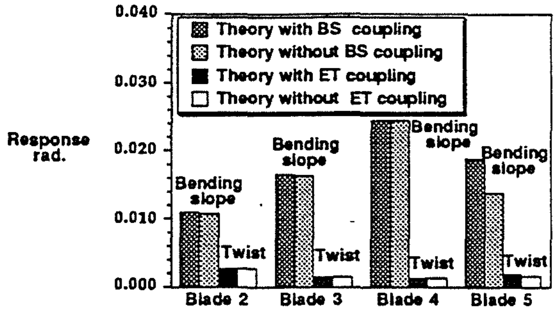

Figure 16. Influence of elastic couplings on response of extension-torsion coupled rotor blades.

As noticed from Figure 11, the maximum value of extension-induced twist at 1000 lbs. is not suitable for tilt-rotor application. The extension-torsion coupling stiffness could be enhanced by increasing the number of layers. Hence, the subsequent blade configurations are examined. Figure 17a shows the twist rate of blades 6 to 8 under axial force. Blade 6 consists of $[0/15]_4$ spar and ±15 skin. Blade 7 consists of $[0/30]_4$ spar and ±30 skin. Blade 8 has $[0/45]_4$ spar and ±45 skin. 0° layers are introduced in the spar lay-ups to reduce the initial twist due to high temperatures during the curing process. Note that the induced twist rate decreases with an increase in fiber orientation from 15° to 45°.

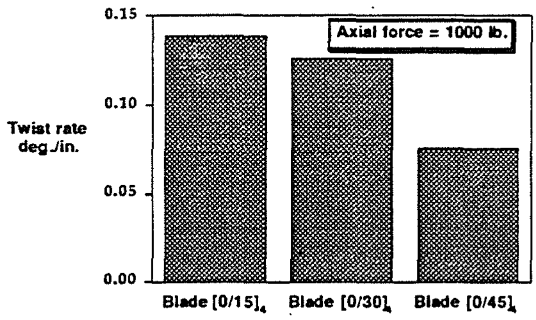

Fig. 17a. Twist rate of extension-torsion coupled rotor blades under axial force.

Figure 17b shows the induced twist rate of blades 9, 10, 11 and 5 under axial force. Blade 9 consists of $[15]_8$ spar and ±15 skin. Blade 10 consists of $[30]_8$ spar and ±30 skin. Blade 11 has $[45]_8$ spar and ±45 skin. It is important to note that the induced twist rate for these blades increases with an increase in fiber orientation from 15° to 45°. However, these lay-up designs are not acceptable as the blades develop large twist due to high curing temperatures. The hygrothermally stable lay-up [20,-70] Ref. [20] provides the induced twist rate of 0.217 deg./in at axial force of 1000 lbs. This value may be useful in satisfying the requirement for the design of extension-twist coupled tilt rotor blades JVX and XV-15 rotors [Ref 19].

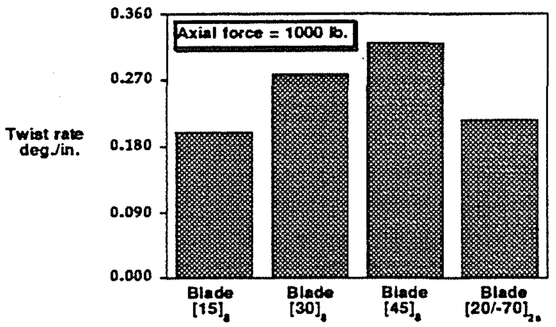

Fig. 17b. Twist rate of extension-torsion coupled rotor blades under axial force.

Conclusions

Two-cell rotor blades made out of general composite laminates were analyzed using Vlasov theory. Transverse shear deformation of the cross-section of the blade was included in the analysis. In order to provide the experimental correlation to the analysis, graphite-epoxy rotor blades with D-spar and skin were fabricated using a matched-die molding technique. These blades were tested for elastic response under bending and torsion loads. Good correlation between analysis and experiment was achieved. Based on this study, the following conclusions are made:

1. The influence of bending-transverse shear and extension-torsion coupling on the structural behavior of coupled blades is controlled by lay-up.

2. The induced twist rate of the order of 0.217 degree per inch length in blade $[20/-70]_{2s}$ can be created by an axial load of 1000 lbs. This makes these coupled blades suitable for tilt-rotor design.

3. The two-cell analysis predicts higher bending and torsional stiffnesses in comparison with the single-cell analysis.

Acknowledgements

This research work was supported by the Army Research Office under contract number DAAL-03-88-C-022, Technical Monitors, Dr. Robert Singleton and Dr. Tom Doligalski.

References

1. Johnson, A. F., "Bending and Torsion of Anisotropic Beams," *International Journal of Solids and Structures*, Vol. 9, pp. 527-551, 1973.

2. Minguet, P., and Dugundji, J., "Experiments and Analysis for Composite Blades under Large Deflections Part 1: Static Behavior, *AIAA Journal*, Vol. 28 (9), pp 1573-1579, September 1990.

3. Minguet, P., and Dugundji, J., "Experiments and Analysis for Composite Blades under Large Deflections Part 2: Dynamic Behavior, *AIAA Journal*, Vol. 28 (9), pp 1580-1588, September 1990.

4. Laulusa, A., "Theoretical and Experimental Investigation of the Large Deflections of Beams," Proceedings of the International Technical Specialists' Meeting on Rotorcraft Basic Research, Atlanta, Georgia, March 25-27, 1991.

5. Chandra, R. and Chopra, I., "Experimental and Theoretical Analysis of Composite I-beams with Elastic Couplings", Proceedings of the 32nd AIAA/ASME/ASCE/AHS/ASC Structures, Structural Dynamics and Materials Conference, AIAA, Washington, DC, April 1991.

6. Chandra, R. and Chopra, I., "Experimental and Theoretical Analysis of Composite I-beams with Elastic Couplings", Accepted for publication in *AIAA Journal.*

7. Chandra, R. and Chopra, I., "Vibration Characteristics of Composite I-Beams with Elastic Couplings Under Rotation", Proceedings of the 47th Annual Forum of American Helicopter Society, Phoenix, Arizona, May 6-8, 1991.

8. Vlasov, V. Z., "Thin-Walled Elastic Beams," Translated from Russian, 1961, National Science Foundation and Department of Commerce, USA.

9. Gjelsvik, A., "The Theory of Thin-Walled Bars," John Wiley & Sons, New York, 1981.

10. Rehfield, L. W. and Atilgan, A. R., "On the Buckling Behavior of Thin Walled Laminated Composite Open Section Beams," Proceedings of the 30th AIAA/ASME/ ASCE/AHS/ASC Structures, Structural Dynamics and Materials Conference, AIAA Washington, DC, April 1989.

11. Hong, C.H. and Chopra, I., "Aeroelastic Stability of a Composite Blade,"*Journal of the American Helicopter Society*, Vol. 30, No. 2, 1985, pp.57-67.

12. Chandra, R., Stemple, A.D. and Chopra, I., "Thin-Walled Composite Beams under Bending, Torsional and Extensional Loads," *Journal of Aircraft*, Vol. 27 (7), 1990, pp 619-627.

13. Smith, E.C. and Chopra, I., "Formulation and Evaluation of an Analytical Model for Composite Box Beams," *Journal of the American Helicopter Society*, Vol. 36(3), pp. 23-35, July 1991.

14. Chandra, R. and Chopra, I., "Experimental-Theoretical Investigation of the Vibration Characteristics of Rotating Composite Box Beams," Accepted for publication in the *Journal of Aircraft*.

15. Rehfield, L. W., A.R. Atilgan and D.H. Hodges," Nonclassical Behavior of Thin-Walled Composite Beams with Closed Cross-Sections", *Journal of American Helicopter Society*, Vol. 35 (2), 1990.

16. Hodges, D.H., Atilgan, A.R., Fulton, M.V. and Rehfield, L.W., "Free-vibration Analysis of Composite Beams," *Journal of American Helicopter Society*, Vol. 36 (3), pp. 36-47, July 1991.

17. Rehfield, L. W., Atilgan, A. R. and Hodges, D. H., "Structural Modeling for Multicell Composite Rotor Blades," Proceedings of the 28th AIAA/ASME/ ASCE/AHS/ASC Structures, Structural Dynamics and Materials Conference, AIAA Washington, DC, April 1988.

18. Kosmatka, J. B., "Extension-Bend-Twist Coupling Behavior of Thin-walled Advanced Composite Beams with Initial Twist," Proceedings of the 32nd AIAA/ASME/ASCE/AHS/ASC Structures, Structural Dynamics and Materials Conference, AIAA, Washington, DC, April 1991.

19. Nixon, M. W., "Extension-Twist Coupling of Composite Circular Tubes with Application to Tilt Rotor Blade Design," Proceedings of the 28th AIAA/ASME/ ASCE/AHS/ASC Structures, Structural Dynamics and Materials Conference, AIAA Washington, DC, April 1987.

20. Winckler, S. J., "Hygrothermally Curvature Stable Laminates with Tension-Torsion Coupling," *Journal of American Helicopter Society*, Vol. 30 (3), July 1985.

Appendix A: Stiffness Matrix K of Blade

$$A_{ij} = \sum_{k=1}^{\#\text{ of layers}} Q_{ij}^{(k)} (h_{k+1} - h_k) \tag{A1}$$

$$B_{ij} = \frac{1}{2} \sum_{k=1}^{\#\text{ of layers}} Q_{ij}^{(k)} (h^2_{k+1} - h^2_k) \tag{A2}$$

$$D_{ij} = \frac{1}{3} \sum_{k=1}^{\#\text{ of layers}} Q_{ij}^{(k)} (h^3_{k+1} - h^3_k) \tag{A3}$$

where $Q_{ij}^{(k)}$ refers to stiffness matrix of k^{th} layer or web in sz plane. h_{k+1} and h_k are coordinates of k^{th} layer in 'n' direction from mid plane of laminates as reference surface.

$$K_{11} = \int_s A_{11}\, ds \qquad (A4)$$

$$K_{12} = \int_s [yA_{11} + \cos\theta\, B_{11}]\, ds \qquad (A5)$$

$$K_{13} = \int_s [xA_{11} - \sin\theta\, B_{11}]\, ds \qquad (A6)$$

$$K_{14} = -\int_s [\varphi A_{11} + qB_{11}]\, ds \qquad (A7)$$

$$K_{15} = \int_s \left[-2B_{16} + \frac{A_{16}G_s}{G\,t}\right] ds \qquad (A8)$$

$$K_{16} = \int_s A_{16}\cos\theta\, ds \qquad (A9)$$

$$K_{17} = \int_s A_{16}\sin\theta\, ds \qquad (A10)$$

$$K_{18} = \int_s B_{11}\sin\theta\, ds \qquad (A11)$$

$$K_{19} = -\int_s B_{11}\cos\theta\, ds \qquad (A12)$$

$$K_{22} = \int_s \left[A_{11}\; y^2 + 2\, B_{11}\, y\cos\theta + D_{11}\cos^2\theta\right] ds \qquad (A13)$$

$$K_{23} = \int_s [A_{11}\, x\, y + 2\, B_{11}\, x\cos\theta - B_{11}\, y\sin\theta - D_{11}\cos\theta\sin\theta]\, ds \qquad (A14)$$

$$K_{24} = \int_s [-(B_{11}\, q\, y) - A_{11}\,\varphi\, y - D_{11}\, q\cos\theta - B_{11}\,\varphi\cos\theta]\, ds \qquad (A15)$$

$$K_{25} = \int_s \left[-2\, B_{16}\, y + \frac{A_{16}\, G_s\, y}{G\,t} - 2\, D_{16}\cos\theta + \frac{B_{16}\, G_s\cos\theta}{G\,t}\right] ds \qquad (A16)$$

$$K_{26} = \int_s [y\cos\theta\, A_{16} + \cos^2\theta\, B_{16}]\, ds \qquad (A17)$$

$$K_{27} = \int_s [y\sin\theta\, A_{16} + \sin 2\theta\, B_{16}/\, 2]\, ds \qquad (A18)$$

$$K_{28} = \int_s [yB_{11} + \cos\theta\, D_{11}]\sin\theta\, ds \qquad (A19)$$

$$K_{29} = -\int_s [(yB_{11} + \cos\theta\, D_{11})\cos\theta]\, ds \qquad (A20)$$

$$K_{33} = \int_s \left[A_{11}\, x^2 - 2\, B_{11} x\sin\theta + D_{11}\sin^2\theta\right] ds \qquad (A21)$$

$$K_{34} = \int_s \left[-B_{11}\, q\, x - A_{11}\, \varphi\, x + D_{11}\, q \sin\theta + B_{11}\, \varphi \sin\theta\right] ds \qquad (A22)$$

$$K_{35} = \int_s \left[-2\, B_{16}\, x + 2\, D_{16} \sin\theta + \frac{A_{16}\, G_s\, x}{G\, t} - \frac{B_{16}\, G_s \sin\theta}{G\, t}\right] ds \qquad (A23)$$

$$K_{36} = \int_s [x\cos\theta\, A_{16} - \sin 2\theta\, B_{16}/\, 2]\, ds \qquad (A24)$$

$$K_{37} = \int_s [x\sin\theta\, A_{16} - \sin^2\theta\, B_{16}]\, ds \qquad (A25)$$

$$K_{38} = \int_s [(xB_{11} - \sin\theta\, D_{11}) \sin\theta]\, ds \qquad (A26)$$

$$K_{39} = -\int_s [\, (xB_{11} - \sin\theta\, D_{11}) \cos\theta]\, ds \qquad (A27)$$

$$K_{44} = \int_s \left[D_{11}\, q^2 + 2\, B_{11}\, q\, \varphi + A_{11}\, \varphi^2\right] ds \qquad (A28)$$

$$K_{45} = \int_s \left[2\, D_{16}\, q + 2\, B_{16}\, \varphi - \frac{B_{16}\, G_s\, q}{G\, t} - \frac{A_{16}\, G_s \varphi}{G\, t}\right] ds \qquad (A29)$$

$$K_{46} = -\int_s [(\varphi A_{16} + q\, B_{16}) \cos\theta]\, ds \qquad (A30)$$

$$K_{47} = -\int_s [(\varphi A_{16} + q\, B_{16}) \sin\theta]\, ds \qquad (A31)$$

$$K_{48} = -\int_s [(B_{11}\varphi + D_{11}q) \sin\theta]\, ds \qquad (A32)$$

$$K_{49} = \int_s [(B_{11}\varphi + D_{11}q) \cos\theta]\, ds \qquad (A33)$$

$$K_{55} = \int_s \left[4\, D_{66} + \frac{A_{66}\, G_s^{\,2}}{(G\, t)^2} - \frac{4\, B_{66}\, G_s}{G\, t}\right] ds \qquad (A34)$$

$$K_{56} = \int_s \left[-2\, B_{66} \cos\theta + \frac{A_{66}\, G_s \cos\theta}{G\, t}\right] ds \qquad (A35)$$

$$K_{57} = \int_s \left[-2\, B_{66} \sin\theta + \frac{A_{66}\, G_s \sin\theta}{G\, t}\right] ds \qquad (A36)$$

$$K_{58} = \int_s \left[-2\, D_{16} \sin\theta + \frac{B_{16}\, G_s \sin\theta}{G\, t}\right] ds \qquad (A37)$$

$$K_{59} = \int_s \left[-2\, D_{16} \cos\theta - \frac{B_{16}\, G_s \sin\theta}{G\, t}\right] ds \qquad (A38)$$

$$K_{66} = \int_s A_{66} \cos^2\theta\, ds \qquad (A39)$$

$$K_{67} = \frac{1}{2}\int_s A_{66} \sin 2\theta \, ds \tag{A40}$$

$$K_{68} = \frac{1}{2}\int_s B_{16} \sin 2\theta \, ds \tag{A41}$$

$$K_{69} = -\int_s B_{16} \cos^2 \theta \, ds \tag{A42}$$

$$K_{77} = \int_s A_{66} \sin^2 \theta \, ds \tag{A43}$$

$$K_{78} = \int_s B_{16} \sin^2 \theta \, ds \tag{A44}$$

$$K_{79} = -\frac{1}{2}\int_s B_{16} \sin 2\theta \, ds \tag{A45}$$

$$K_{88} = \int_s \left[D_{11} \cos\theta \sin\theta\right] ds \tag{A46}$$

$$K_{89} = \int_s \left[-D_{11} \cos^2\theta\right] ds \tag{A47}$$

$$K_{99} = \int_s \left[-D_{11} \cos\theta \sin\theta\right] ds \tag{A48}$$

For computation of 45 coefficients of [K] matrix for a general situation, the contour integration for airfoil section needs to be carried out.

Table 1: Details of Composite Blades

Length = 28 in.; Width = 3 in.; Thickness = 0.36 in.
NACA 0012 aerofoil
Material: Graphite-epoxy
$E_\ell = 19\text{x}10^6$ psi; $E_t = 1.35\text{x}10^6$ psi; $G_{\ell t} = 0.85\text{x}10^6$ psi; $\mu_{\ell t} = 0.40$
Ply thickness=0.005 in.

Cases	D-spar Top flange	D-spar Bottom Flange	D-spar Web	Skin	Coupling
Blade 1	$[0]_4$	$[0]_4$	$[0]_4$	[15 / -15]	E-T
Blade 2	$[0/15]_2$	$[0/15]_2$	$[0/15]_2$	[15 / -15]	E-T
Blade 3	$[0/30]_2$	$[0/30]_2$	$[0/30]_2$	[30 / -30]	E-T
Blade 4	$[0/45]_2$	$[0/45]_2$	$[0/45]_2$	[45 / -45]	E-T
Blade 5	$[20/-70]_{2s}$	$[20/-70]_{2s}$	$[20/-70]_{2s}$	[20/-70]	E-T
Blade 6	$[0/15]_4$	$[0/15]_4$	$[0/15]_4$	[15 / -15]	E-T
Blade 7	$[0/30]_4$	$[0/30]_4$	$[0/30]_4$	[30 / -30]	E-T
Blade 8	$[0/45]_4$	$[0/45]_4$	$[0/45]_4$	[45 / -45]	E-T
Blade 9	$[15]_8$	$[15]_8$	$[15]_8$	[15 / -15]	E-T
Blade 10	$[30]_8$	$[30]_8$	$[30]_8$	[30 / -30]	E-T
Blade 11	$[45]_8$	$[45]_8$	$[45]_8$	[45 / -45]	E-T

E-T = Extension-twist